Optical and mechanical designs of the multi-band SWIR receiver for the Lunar Flashlight CubeSat mission

Quentin Vinckier[a], Karlton Crabtree[b], Megan Gibson[c], Christopher Smith[c], Udo Wehmeier[a], Paul O. Hayne[d], R. Glenn Sellar[a]

[a]Jet Propulsion Laboratory, California Institute of Technology, 4800 Oak Grove Dr, Pasadena, CA, USA 91109; [b]Photon Engineering LLC, 310 S Williams Blvd #222, Tucson, AZ, USA 85711; [c]Sierra Lobo Inc., 102 Pinnacle Drive, Fremont, OH, USA 43420; [d]University of Colorado, 391 UCB, Boulder, CO, USA 80309

ABSTRACT

Mapping and quantifying lunar water ice addresses one of NASA's Strategic Knowledge Gaps to understand the lunar resource potential for future human exploration of the Moon. Lunar Flashlight is an innovative NASA CubeSat mission dedicated to mapping water ice in the permanently-shadowed and occasionally-sunlit regions in the vicinity of the lunar South Pole. Lunar Flashlight will acquire these measurements from lunar orbit using a multi-band laser reflectometer composed of an optical receiver aligned with four lasers emitting different wavelengths in the shortwave infrared spectral region between 1 µm and 2 µm. The receiver measures the laser radiance reflected from the lunar surface in each spectral band and continuum/absorption reflectance band ratios are then analyzed to quantify water ice concentration in the illuminated spot. The receiver utilizes a 70×70-mm, aluminum, off-axis paraboloidal mirror with a focal length of 70 mm, which collects the incoming light onto a single, 2 mm diameter InGaAs detector with a cutoff wavelength of 2.4 µm. We present the optical and mechanical designs of the receiver, including its optimization for rejection of solar stray-light from outside its intended field of view. This highly mass- and volume-constrained instrument payload will demonstrate several firsts, including being one of the first instruments onboard a CubeSat performing science measurements beyond low Earth orbit and the first planetary mission to use multi-band active reflectometry from orbit.

Keywords: Lunar Flashlight, reflectometer, reflectometry, CubeSat, radiometry, radiometer, laser remote sensing

1. INTRODUCTION

For nearly a century, predictions have been made for the existence of stable ice deposits in the permanently shadowed craters of the Moon[1,2]. In such craters located near the lunar poles, temperatures are low enough (<110 K) to trap volatiles, such as H_2O, NH_3, CO_2 or H_2S, in their solid state for up to billions of years[3–5]. Mapping and quantifying lunar volatiles, in particular water, associated with these cold traps addresses one of NASA's (National Aeronautics and Space Administration) Strategic Knowledge Gaps (SKG) to understand the lunar resource potential for future human and robotic exploration of the moon[6]. In addition, these data are also crucial to address outstanding questions in planetary science, such as testing hypotheses regarding the delivery and retention of water and other volatiles in the inner Solar System.

Over the past two decades, several orbital and flyby missions have revealed strong indications of the presence of lunar water ice using a wide range of techniques[7–27]. Due to limitations of the measurements thus far acquired, interpretations are varied and no consensus has yet been achieved as to the form, quantity, or distribution of lunar H_2O at concentrations sufficient for in-situ resource utilization (ISRU)[3,5,13,25]. The Lunar Flashlight (LF) spacecraft is a '6U' (i.e. 6-unit with dimensions ~10×20×30 cm) CubeSat designed to orbit the Moon to detect, quantify, and map from lunar H_2O ice in the permanently-shadowed regions and occasionally-sunlit regions of the Moon for potential ISRU. LF's instrument, a multi-band reflectometer, will measure zero-phase-angle surface reflectance at four different wavelength bands between 1 µm and 2 µm in the shortwave infrared (SWIR) wavelength region[28,29]. One of these bands, the 1.064 µm band, has been chosen to enable comparison with data acquired by the Lunar Orbiter Laser Altimeter (LOLA)[25–28, 30–32]. LF will be one of the first CubeSats performing science measurements beyond low Earth orbit (two other CubeSat missions have been selected to make complementary lunar volatile measurements[33,34]) and the first planetary mission to use multi-band active reflectometry from orbit.

2. INSTRUMENT AND MEASUREMENT APPROACH

The science goal is to identify locations where water ice is present at concentrations ≥ 0.5 wt% on the lunar surface with a mapping resolution of 1-2 km (10 km for the minimum success criteria). To achieve this goal, the LF instrument (a '2U' active multi-band reflectometer, depicted in Figure 1) employs an optical receiver aligned with four high-power diode lasers, each emitting in a different wavelength band in the 1-2 µm SWIR spectral region.

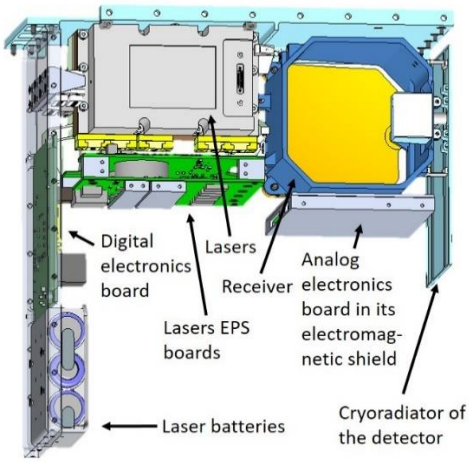

Figure 1. Lunar Flashlight multi-band SWIR reflectometer. The diode lasers, pumped at 45 A supplied by the laser electrical power system (EPS) board & laser batteries, output optical power from 15 to 73 W in the 1-2 µm SWIR spectral region. > 99.6% of the emitted energy is encircled within a full-angle of 17 mrad. The receiver – based on an off-axis bare aluminum paraboloid mirror which collects the incoming light onto a single-pixel InGaAs detector – has been designed to maximize detection efficiency and uniformity within 20 mrad field of view (FOV). A cryoradiator thermally coupled to the receiver detector cools the detector down to -65°C during science data paths. An analog electronic board – tuned to maximize the signal-to-noise ratio (SNR) for the available data set – amplifies and reads the detector signal at 100 kHz. The detector analog signal is then digitized by the digital electronics board.

As depicted in Figure 2, two out of the four wavelengths (~1.495 µm and ~1.99 µm) correspond to peak absorption for water ice, while the two other wavelengths (~1.064 µm and ~1.85 µm) correspond to nearby continuum.

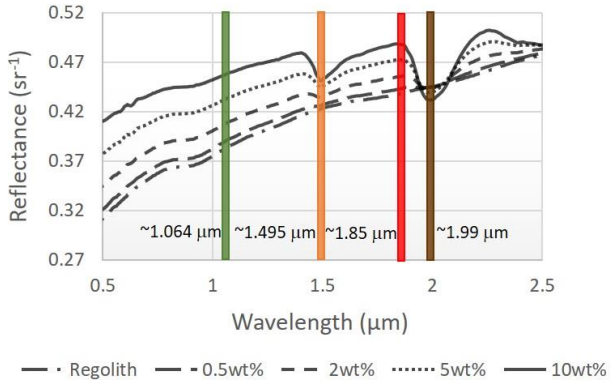

Figure 2. Reflectance spectrum (bidirectional reflectance) for different water ice contents in lunar regolith at zero phase angle. We calculated these model spectra using Hapke theory[35], with water ice optical constants from Warren et al.[36] and a reflectance spectrum of Apollo 14 lunar highlands sample 14259-85.

The lasers fire sequentially for 1-5 ms each, followed by a pause of 1-5 ms with all lasers off. The optical receiver collects and measures a portion of the light reflected from the lunar surface. The measurement with all lasers off quantifies the background, which is the sum of detector dark current, thermal emission from the receiver itself incident on the science

detector, and solar illumination reflected from the lunar surface and detected by the instrument from both inside and outside its field of view (FOV). The instrument background is subtracted in post-processing from the measured signals. In order to increase the signal-to-noise ratio (SNR), the measurements are averaged for each of the spectral band over the time in which the laser-illuminated FOV moves a distance on the lunar surface corresponding to the desired mapping resolution of lunar water ice (1-10 km). We derive the reflectance of the lunar surface at each of the four wavelengths and continuum/absorption reflectance band ratios are then analyzed to quantify the weight percent of water ice (wt%) in the illuminated FOV. During the planned 2-month primary mission, LF will pulse the lasers for 1-3 minutes from ten ~5.5 days near-rectilinear orbits planned, at altitudes of 12.6-52.4 km within 10° latitude of the lunar South Pole. The mission overview is depicted in Figure 3.

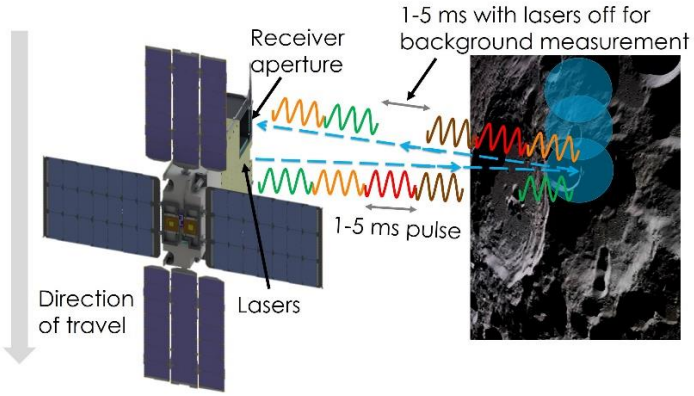

Figure 3. Lunar Flashlight CubeSat mission overview.

3. OPTOMECHANICAL DESIGN OF THE RECEIVER

3.1 Receiver optical design

The volume and mass limitations of a CubeSat constrain the receiver design to be as simple as possible. Out of the 2U volume allocated to the instrument, a 1U volume (approximately 10×10×10 cm^3) is suballocated to the receiver. The optical design is a single, off-aperture, 70×70-mm aluminum paraboloidal mirror with a single-pixel detector located at the focus of the mirror. The initial optical design of the receiver (performed by Photon Engineering, LLC using the FRED software package) was described by Vinckier et al.[37]. Here, we present the completed and detailed optical, mechanical, and thermal design of the receiver.

To set requirements for the optical design of the receiver, an instrument system engineering effort determined the optimal receiver FOV. We define the receiver FOV as the incident angle range within which the detection efficiency is maximal and sufficiently uniform (< 1% non-uniformity). In the instrument system design, > 99.6% of the emitted energy by the lasers is encircled within a full-angle of 17 mrad[37]. This laser divergence specification drives the required receiver FOV. On one hand, the receiver FOV has to cover at least the angular profile of the emitted laser power, in order to minimize the sensitivity of the received signal to changes in alignment between the laser beam profiles and the receiver FOV. On the other hand, the receiver FOV cannot be set to an arbitrarily high value because we have to minimize the background (including detected solar light) in order to maximize the instrument SNR[28,29,37]. We designed the receiver to provide a FOV of 20 mrad. Using the paraxial approximation, the theoretical FOV of an optical system with a detector located at the focal position is given by FOV=2×atan[D/(2f)], where D is the diameter of the detector and f is the effective focal length of the mirror. However the very fast focal ratio (f < 100 mm due to volume constraints) leads to large aberrations. This means that the paraxial approximation mentioned above can no longer be used to estimate the required focal length and detector diameter in order to provide the 20 mrad FOV. A ray-tracing software package "FRED" was employed to evaluate the receiver FOV as a function of detector diameter and focal length. The detector was selected from those available off-the-shelf from Teledyne Judson Technologies: circular InGaAs detectors available with 2.4 μm cutoff wavelength in five different diameters (0.25, 0.5, 1, 2, and 3 mm). The detector diameter has to be as small as possible to minimize the noise

generated by the detecting chain, which constitutes the main contribution in the instrument error budget[29]. FRED simulations show that a minimum detector diameter of 2 mm is necessary to reach a sufficiently-uniform detection efficiency within 20 mrad for this volume-constrained optical design. The resulting optimal focal length is 70 mm.

The second step of the optical design phase was to design baffles to minimize stray solar light incident on the detector active area, i.e. the solar illumination of the lunar surface reflected towards the receiver aperture and scattered onto the detector active area from outside the FOV. The stray light scattering model used by the FRED software is based on the Harvey-Shack surface scatter theory[38]. All internal surfaces are painted with flat black paint and the mirror was modeled as 30 Å roughness and CL600[39] particulates (0.696% percent area coverage).

In order to estimate the science performance of a given receiver optical design as a function of the predicted orbits and lunar surface illumination, our mission-level performance model uses the receiver point source transmittance (PST) function calculated in FRED[28]. This is effectively the fraction of flux at the receiver aperture that reaches the detector active area as a function of the θ_x and θ_Z incident field angles, where θ_x and θ_z are respectively the rotation angles around axis X and Z, XZ plane being perpendicular to the receiver optical axis. The PST thus represents the receiver detection efficiency as a function of θ_x and θ_z. Different configurations were analyzed with our mission performance model to derive the optimized receiver optical design depicted in Figure 4. Figure 5 shows the predicted rotational average of the PST function (used in our mission-level performance model) corresponding to the final receiver optomechanical design presented in section 3.2. Figure 6 depicts the central portion of the 2D PST function for small θ_x and θ_Z incident angles to illustrate the receiver FOV. Table 1 lists the principal technical specifications of the receiver design.

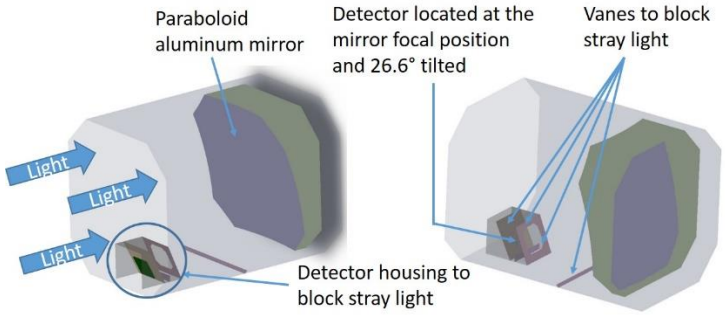

Figure 4. Receiver optical design.

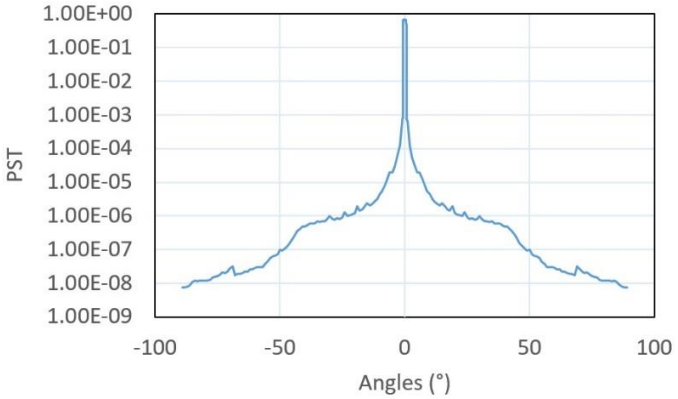

Figure 5. Rotationally averaged receiver point source transmittance (PST) function. The maximum value of the PST is equal to 0.68 (68% of the light at the receiver aperture reaches the detector active area), which is significantly less than 1. The primary reason for this is that the PST calculation is normalized to the flux passing through an unobscured 75 mm square entrance aperture, rather than the smaller and more complex mirror shape of the actual receiver. Additional power losses come from the mirror reflectivity modeled as 94.5% (reflectance of Al at a wavelength of 1 µm), the detector surface reflectivity modeled as 3%, and losses due to vignetting by the detector housing (which obstructs a part of the receiver aperture).

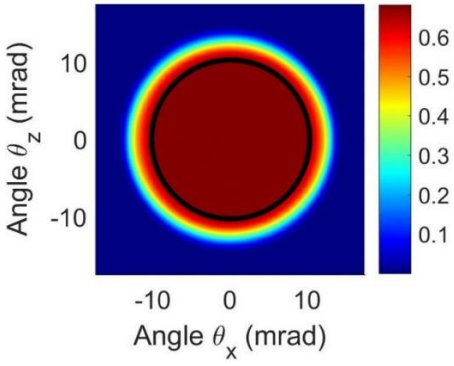

Figure 6. Receiver FOV. The color scale corresponds to the fraction of photons at the receiver aperture reaches the detector active area. θ_x and θ_Z are the incident field angles: they represent respectively the rotation angles around axis X and Z, XZ plane being perpendicular to the receiver optical axis. The black circle represents the 20 mrad receiver FOV.

Table 1. Principal technical specifications of the current receiver design.

Receiver dimensions	100×75×75 mm
Receiver aperture	75×75 mm
Mirror surface	• 70×70 mm bare aluminum off-axis paraboloid mirror, post-polish • Radius of curvature: 140 mm • Surface accuracy: 2λ @ 632.8 nm • RMS roughness: <30 Å
Detector	• 2.4 µm cutoff InGaAs Teledyne Judson 2 mm diameter detector • Thermally isolated from the receiver structure and cooled at -65°C by a cryoradiator thermally stabilized by a PID (proportional–integral–derivative)-controlled heater (the cryradiator is not shown on Figure 4; see Figure 8)

The instrument will be calibrated on earth when the receiver and the laser package are aligned. Changes in alignment between the receiver and the laser package during the mission will induce an error in the detected signal because this changes the overlap between the laser divergence profiles and the receiver FOV depicted in Figure 6. Based on the predicted receiver PST and laser divergence profiles, we have calculated the worst-case detected signal error Δ as a function of the receiver-to-laser package misalignment following the method described by Vinckier et al.[37]. Results of this analysis are depicted in Figure 7.

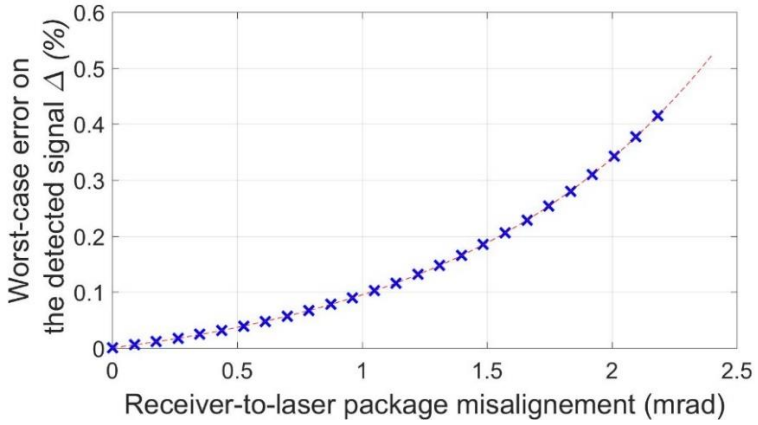

Figure 7. Worst-case error on the detected signal as a function of the receiver-to-laser package misalignment.

3.2 Receiver mechanical design

The optical design defines only the dimensions and the relative positions of the front surface of the mirror, the detector, and the stray light control elements (receiver housing, baffles, vanes). Our mechanical design (created by Sierra Lobo Inc.) defines all the remaining dimensions, materials, and processes to a level of detail that supports fabrication and integration of the complete receiver.

The LF instrument optomechanical design, depicted in Figure 8, comprises two subsystems: the laser and receiver modules. The former consists of multiple lasers, collimation lenses and related hardware contained in an enclosure with copper heatsink, which is bolted to an aluminum alloy chassis containing phase-change material (PCM). This PCM chassis does not only provide the means to stable laser temperature during operation, but it also forms the mechanical foundation for the receiver module.

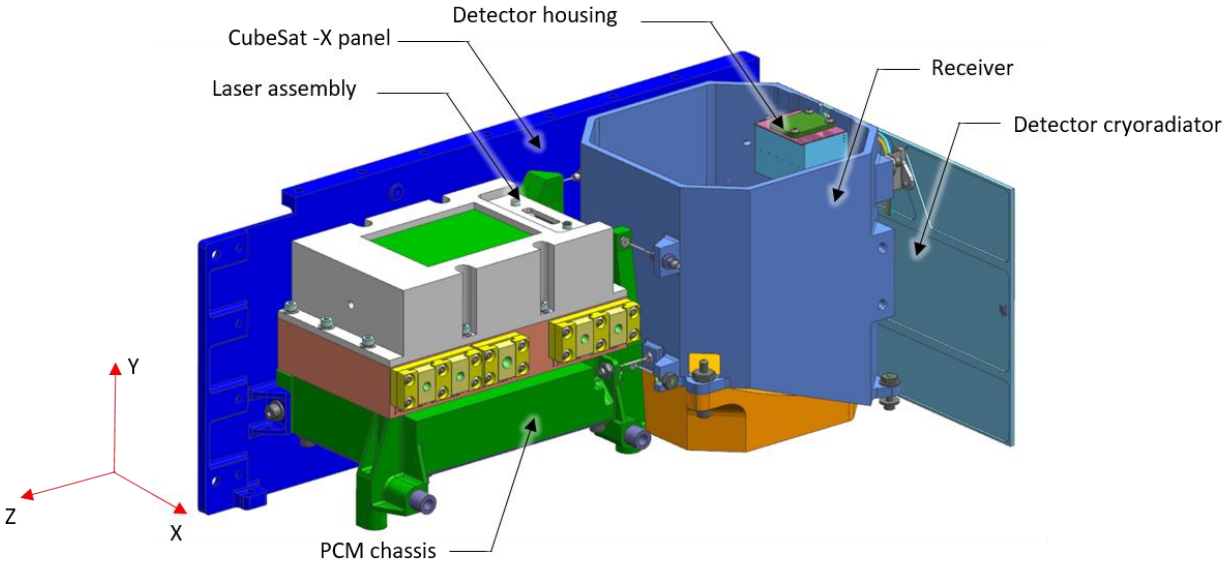

Figure 8. LF reflectometer optomechanical assembly. The assembled reflectometer optomechanical assembly is attached semi-kinematically through the rigid PCM chassis mounting features to the -X and -Y structural panels of the spacecraft.

The receiver module has an octagonal aperture, fastened to a machined aluminum housing. First-order athermalization is achieved through the shared use of aluminum alloy 6061-T6 between the post-polished, diamond-turned, off-axis paraboloidal mirror and the receiver housing. The mirror's mounting pads are diamond-turned to their final profile in the same lathe operation as used to machine the optical surface, providing a high degree of precision in the pad co-planarity/parallelism. The pads that interface the mirror to the receiver housings are similarly diamond turned in one lathe operation. Mirror-to-receiver-housing location is maintained through a close slip-fit sleeve with a concentric fastener. This alignment feature is coincident with the mirror optical axis and functions as the primary tooling feature for turning operations. A secondary slotted hole on one of the other mounting pads uses a similar sleeved fastener to control clocking of the mirror. The combination of these features allows an adjustment-free "snap together" integration approach (see Figure 9).

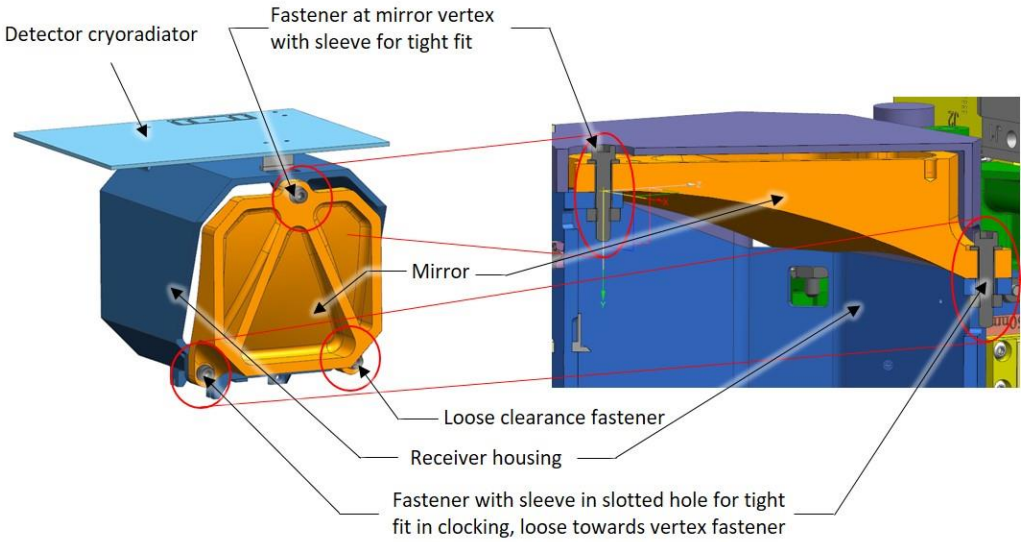

Figure 9. Receiver module with cryoradiator (left) and section view (right) showing fastener detail of semi-kinematic snap-together design. The external surfaces of the receiver housing are electro-plated with gold to provide passive cooling.

The receiver's InGaAs detector sits at prime focus, bonded to a molybdenum alloy post to conduct heat to an adjacent titanium flexure-mounted cryoradiator. This post is epoxy bonded into a titanium alloy detector housing, which provides the necessary thermal isolation from the receiver housing. The detector housing uses a semi-kinematic 3-2-1 screw attachment to the receiver housing (see Figure 10). The planes of the mating surfaces are oriented so that they provide athermal detector positioning, given the mixed materials in the assembly. The detector position relative to the mirror is set by machine tolerances at the mirror to receiver housing interface, and by shim thickness at the detector to housing interface. Dimensional inspection data for each of the components in the mechanical path between mirror and detector will be collected and reduced into shim values to achieve a nominal detector position.

The detector housing is a two-piece clamshell assembly fabricated from the previously mentioned titanium alloy. Baffle features are machined into both halves of the assembly. A small circular baffle is bonded to one of the internal housing surfaces just above the detector surface. This additional piece is required to achieve the baffle profile and orientation prescribed by stray light analysis results. Internal surfaces are painted with Aeroglaze Z-306 black prior to patch-bonding the halves together with injected epoxy. External surfaces are similarly painted with Aeroglaze Z-306 black.

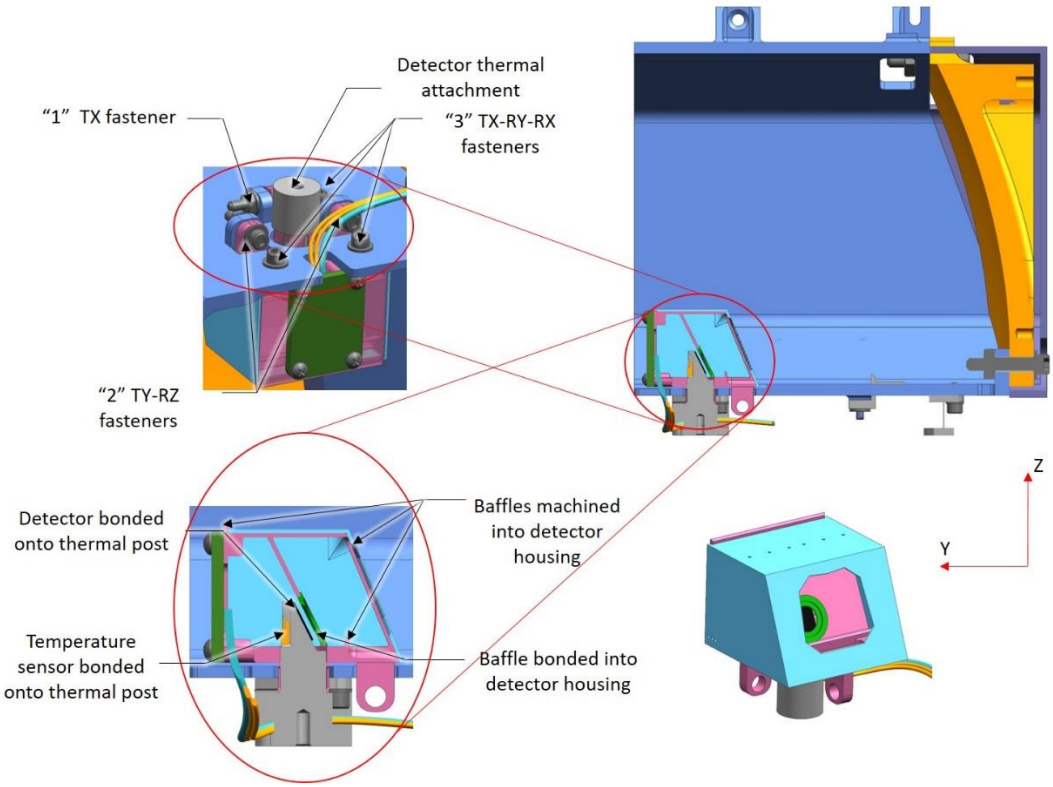

Figure 10. Detector semi-kinematic attachment to the receiver housing (top left), detector assembly section view (lower left), receiver section view (top right), and alone detector assembly 3D view (lower right).

The mechanical connection between the receiver and laser modules is achieved via six titanium-alloy rod flexures (see Figure 11). These "stingers" provide compliant attachment as well as thermal isolation between the laser and receiver while maintaining boresight alignment. Limited relative pointing adjustment is achieved by differential shimming between seats machined into the receiver housing, the PCM chassis, and the stingers.

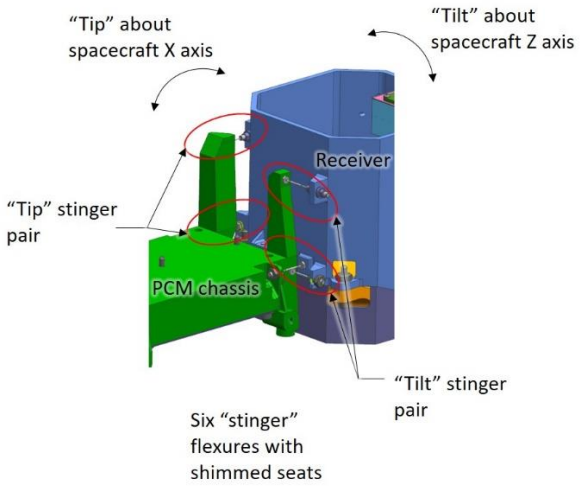

Figure 11. Receiver module to PCM chassis connection showing six stinger flexures with pairs oriented for tip-tilt shim adjustment relative to laser module boresight.

4. CONCLUSIONS

This paper presents the optical and mechanical designs of the Lunar Flashlight receiver, which have been completed to the point that fabrication and integration can now begin. This design meets all the requirements for the receiver module; the next steps will be to manufacture, integrate, align, characterize and calibrate the receiver, followed by the entire instrument.

This highly mass- and volume-constrained instrument payload will demonstrate several firsts, including being one of the first instruments onboard a CubeSat performing science measurements beyond low Earth orbit and the first planetary mission to use multi-band active reflectometry from orbit.

ACKNOWLEDGMENT

The Lunar Flashlight mission is funded by the Advanced Exploration Systems program in the Human Exploration and Operations (HEO) mission directorate of the National Aeronautics and Space Administration (NASA). Part of this work was performed at the Jet Propulsion Laboratory, California Institute of Technology, under contract with NASA.

REFERENCES

[1] Goddard, R. H., [The Papers of Robert H. Goddard: 1898-1924], McGraw-Hill, New York, 413-430 (1970).
[2] Watson, K., Murray, B. and Brown, H., "On the possible presence of ice on the Moon," Journal of Geophysical Research 66(5), 1598-1600 (1961).
[3] Paige, D. A., Siegler, M. A., Zhang, J. A., Hayne, P. O., Foote, E. J., Bennett, K. A., Vasavada, A. R., Greenhagen, B. T., Schofield, J. T., McCleese, D. J., Foote, M. J., DeJong, E., Bills, B. G., Hartford, W., Murray, B. C., Allen, C. C., Snook, K., Soderblom, L. A., Calcutt, S., Taylor, F. W., Bowles, N. E., Bandfield, J. L., Elphic, R., Ghent, R., Glotch, T. D., Wyatt, M. B. and Lucey P. G., "Diviner lunar radiometer observations of cold traps in the Moon's south polar region," Science 330(6003), 479-482 (2010).
[4] Hayne, P. O., Hendrix, A., Sefton-Nash, E., Siegler, M. A., Lucey, P. G., Retherford, K. D., Williams, J. P., Greenhagen, B. T. and Paige, D. A., "Evidence for exposed water ice in the Moon's south polar regions from Lunar Reconnaissance Orbiter ultraviolet albedo and temperature measurements," Icarus 255, 58-69 (2015).
[5] Hayne, P. O., Paige, D. A., Ingersoll, A. P., Judd, M. A., Aharonson, O., Alkali, L., Byrne, S., Cohen, B., Colaprete, A., Combe, J. P. and Edwards, C., "New Approaches to Lunar Ice Detection and Mapping: Study Overview and Results of the First Workshop," Report of the Annual Meeting of the Lunar Exploration Analysis Group 1748, 7043 (2013).
[6] The Lunar Exploration Analysis Group (LEAG), the Mars Exploration Program Analysis Group (MEPAG) and the Small Bodies Assessment Group (SBAG), "Strategic Knowledge Gaps (SKGs)," NASA, 29 August 2016, < https://www.nasa.gov/exploration/library/skg.html > (19 September 2016).
[7] Thomson, B. J., Bussey, D. B. J., Neish, C. D., Cahill, J. T. S., Heggy, E., Kirk, R. L., Patterson, G. W., Raney, R. K., Spudis, P. D., Thompson, T. W. and Ustinov, E. A., "An upper limit for ice in Shackleton crater as revealed by LRO Mini-RF orbital radar," Geophysical Research Letters 39(14) (2012).
[8] Spudis, P. D., Bussey, D. B. J., Baloga, S. M., Cahill, J. T. S., Glaze, L. S., Patterson, G. W., Raney, R. K., Thompson, T. W., Thomson, B. J. and Ustinov, E. A., "Evidence for water ice on the Moon: Results for anomalous polar craters from the LRO Mini-RF imaging radar," Journal of Geophysical Research: Planets 118(10), 2016-2029 (2013).
[9] Nozette, S., Lichtenberg, C. L., Spudis, P., Bonner, R., Ort, W., Malaret, E., Robinson, M. and Shoemaker, E. M., "The Clementine bistatic radar experiment," Science 274(5292), 1495-1498 (2016).
[10] Feldman, W. C., Maurice, S., Binder, A. B., Barraclough, B. L., Elphic, R. C. and Lawrence, D. J., "Fluxes of fast and epithermal neutrons from Lunar Prospector: Evidence for water ice at the lunar poles," Science 281(5382), 1496-1500 (1998).
[11] Feldman, W. C., Lawrence, D. J., Elphic, R. C., Barraclough, B. L., Maurice, S., Genetay, I. and Binder, A. B., "Polar hydrogen deposits on the Moon," Journal of Geophysical Research 105(E2), 4175-4195 (2000).
[12] Feldman, W. C., Lawrence, D. J., Little, R. C., Lawson, S. L., Gasnault, O., Wiens, R. C., Barraclough, B. L., Elphic, R. C., Prettyman, T. H. and Steinberg, J. T., "Evidence for water ice near the lunar poles," Journal of Geophysical Research, 106(E10), 23231-23251 (2001).

[13] Mitrofanov, I. G., Sanin, A. B., Boynton, W. V., Chin, G., Garvin, J. B., Golovin, D., Evans, L. G., Harshman, K., Kozyrev, A. S., Litvak, M. L. and Malakhov, A., "Hydrogen mapping of the lunar south pole using the LRO neutron detector experiment LEND," Science 330(6003), 483-486 (2010).
[14] Mitrofanov, I., Litvak, M., Sanin, A., Malakhov, A., Golovin, D., Boynton, W., Droege, G., Chin, G., Evans, L., Harshman, K. and Fedosov, F., "Testing polar spots of water-rich permafrost on the Moon: LEND observations onboard LRO," Journal of Geophysical Research: Planets 117(E12) (2012).
[15] Boynton, W. V., Droege, G. F., Mitrofanov, I. G., McClanahan, T. P., Sanin, A. B., Litvak, M. L., Schaffner, M., Chin, G., Evans, L. G., Garvin, J. B. and Harshman, K., "High spatial resolution studies of epithermal neutron emission from the lunar poles: Constraints on hydrogen mobility," Journal of Geophysical Research: Planets 117(E12) (2012).
[16] Livengood, T. A., Chin, G., Sagdeev, R. Z., Mitrofanov, I. G., Boynton, W. V., Evans, L. G., Litvak, M. L., McClanahan, T. P., Sanin, A. B. and Starr, R. D., "Evidence for Diurnally Varying Hydration at the Moon's Equator from the Lunar Exploration Neutron Detector (LEND)," Proc. Lunar and Planetary Science Conference 45, 1507 (2014).
[17] Schwadron, N. A., Wilson, J. K., Looper, M. D., Jordan, A. P., Spence, H. E., Blake, J. B., Case, A. W., Iwata, Y., Kasper, J. C., Farrell, W. M. and Lawrence, D. J., "Signatures of volatiles in the lunar proton albedo," Icarus 273, 25-35 (2016).
[18] Gladstone, G. R., Retherford, K. D., Egan, A. F., Kaufmann, D. E., Miles, P. F., Parker, J. W., Horvath, D., Rojas, P. M., Versteeg, M. H., Davis, M. W. and Greathouse, T. K., "Far-ultraviolet reflectance properties of the Moon's permanently shadowed regions," Journal of Geophysical Research: Planets 117(E12) (2012).
[19] Hendrix, A. R., Retherford, K. D., Randall Gladstone, G., Hurley, D. M., Feldman, P. D., Egan, A. F., Kaufmann, D. E., Miles, P. F., Parker, J. W., Horvath, D. and Rojas, P. M., "The lunar far-UV albedo: Indicator of hydration and weathering," Journal of Geophysical Research: Planets 117(E12) (2012).
[20] Colaprete, A., Schultz, P., Heldmann, J., Wooden, D., Shirley, M., Ennico, K., Hermalyn, B., Marshall, W., Ricco, A., Elphic, R. C. and Goldstein, D., "Detection of water in the LCROSS ejecta plume," Science 330(6003), 463-468 (2012).
[21] Heldmann, J. L., Lamb, J., Asturias, D., Colaprete, A., Goldstein, D. B., Trafton, L. M. and Varghese, P. L., "Evolution of the dust and water ice plume components as observed by the LCROSS visible camera and UV–visible spectrometer," Icarus 254, 262-275 (2015).
[22] Pieters, C. M., Goswami, J. N., Clark, R. N., Annadurai, M., Boardman, J., Buratti, B., Combe, J. P., Dyar, M. D., Green, R., Head, J. W. and Hibbitts, C., "Character and spatial distribution of OH/H2O on the surface of the Moon seen by M3 on Chandrayaan-1," Science 326(5952), 568-572 (2009).
[23] Sunshine, J. M., Farnham, T. L., Feaga, L. M., Groussin, O., Merlin, F., Milliken, R. E. and A'Hearn, M. F., "Temporal and spatial variability of lunar hydration as observed by the Deep Impact spacecraft," Science 326(5952), 565-568 (2009).
[24] Clark, R. N., "Detection of adsorbed water and hydroxyl on the Moon," Science 326(5952), 562-564 (2009).
[25] Zuber, M. T., Head, J. W., Smith, D. E., Neumann, G. A., Mazarico, E., Torrence, M. H., Aharonson, O., Tye, A. R., Fassett, C. I., Rosenburg, M. A. and Melosh, H. J., "Constraints on the volatile distribution within Shackleton crater at the lunar south pole," Nature 486(7403), 378-381 (2012).
[26] Lucey, P. G., Neumann, G. A., Paige, D. A., Riner, M. A., Mazarico, E. M., Smith, D. E., Zuber, M. T., Siegler, M., Hayne, P. O., Bussey, D. B. J., Cahill, J. T. S., McGovern, A., Isaacson, P., Corley, L. M., Torrence, M. H., Melosh, H. J., Head, J. W. and Song, E., "Evidence for Water Ice and Temperature Dependent Space Weathering at the Lunar Poles from Lola and diviners," Proc. Lunar and Planetary Science Conference 45, 2325 (2014).
[27] Fisher, E. A., Lucey, P. G., Lemelin, M., Greenhagen, B. T., Siegler, M. A., Mazarico, E., Aharonson, O., Williams, J. P., Hayne, P. O., Neumann, G. A. and Paige, D. A., "Evidence for surface water ice in the lunar polar regions using reflectance measurements from the Lunar Orbiter Laser Altimeter and temperature measurements from the Diviner Lunar Radiometer Experiment," Icarus 292, 74-85 (2017).
[28] Cohen, B. A., Hayne, P. O., Greenhagen, B. T., Paige, D. A., Camacho, J. M., Crabtree, K., Paine, C. G. and Sellar, R. G., "Payload Design for the Lunar Flashlight Mission," Proc. Lunar and Planetary Science Conference 48, 1709 (2017).
[29] Vinckier, Q., Hayne, P. O., Martinez-Camacho, J.M., Paine, C., Cohen, B. A., Wehmeier, U. J., and Sellar, R. G., "System Performance Modeling of the Lunar Flashlight CubeSat Instrument", Proc. Lunar and Planetary Science Conference 49, 1030 (2018).

[30] Smith, D. E., Zuber, M. T., Neumann, G. A., Lemoine, F. G., Mazarico, E., Torrence, M. H., McGarry, J. F., Rowlands, D. D., Head, J. W., Duxbury, T. H. and Aharonson, O., "Initial observations from the lunar orbiter laser altimeter (LOLA)," Geophysical Research Letters 37(18) (2010).
[31] Riris, H., Cavanaugh, J., Sun, X., Liiva, P., Rodriguez, M. and Neuman, G., "The lunar orbiter laser altimeter (LOLA) on NASA's lunar reconnaissance orbiter (LRO) mission," Proc. International Conference on Space Optics 8 (2010).
[32] Ramos-Izquierdo, L., Scott III, V. S., Connelly, J., Schmidt, S., Mamakos, W., Guzek, J., Peters, C., Liiva, P., Rodriguez, M., Cavanaugh, J. and Riris, H., "Optical system design and integration of the Lunar Orbiter Laser Altimeter," Applied Optics 48(16), 3035-3049 (2009).
[33] Clark, P. E., Malphrus, B., Brown, K., Hurford, T., Brambora, C., MacDowall, R., Folta, D., Tsay, M., Brandon, C. and Team, L. I. C., "Lunar Ice Cube: Searching for Lunar Volatiles with a lunar cubesat orbiter," Proc. AAS/Division for Planetary Sciences Meeting 48, 223.03 (2016).
[34] Hardgrove, C., Bell, J., Thangavelautham, J., Klesh, A., Starr, R., Colaprete, T., Robinson, M., Drake, D., Johnson, E., Christian, J. and Genova, A., "The Lunar Polar Hydrogen Mapper (LunaH-Map) mission: Mapping hydrogen distributions in permanently shadowed regions of the Moon's south pole," Proc. Annual Meeting of the Lunar Exploration Analysis Group 1863, 2035 (2015).
[35] Hapke, B., "Bidirectional reflectance spectroscopy: 1. Theory," Journal of Geophysical Research: Solid Earth 86(B4), 3039-3054 (1981).
[36] Warren, S. G., and Richard E. B., "Optical constants of ice from the ultraviolet to the microwave: A revised compilation," Journal of Geophysical Research: Atmospheres 113(D14) (2008).
[37] Vinckier, Q., Crabtree, K., Paine, C. G., Hayne, P. O., and Sellar, G. R., "Design and characterization of a low cost CubeSat multi-band optical receiver to map water ice on the lunar surface for the Lunar Flashlight mission," Proc. SPIE Infrared Remote Sensing and Instrumentation XXV (Vol. 10403), 104030R (2017).
[38] Harvey, J., "Light Scattering Characteristics of Optical Surfaces," Ph.D. dissertation, University of Arizona (1976).
[39] MIL-STD-1246C, MILITARY STANDARD: PRODUCT CLEANLINESS LEVELS CONTAMINATION CONTROL PROGRAM, 1994.